LANGMUIR

pubs.acs.org/Langmuir Article

Protonation-Driven Aqueous Lyotropic Self-Assembly of Synthetic Six-Tail Lipidoids

James Jennings, Matthew C. D. Carter, Chang Yun Son, Qiang Cui, David M. Lynn, and Mahesh. K. Mahanthappa*

Cite This: *Langmuir* 2020, 36, 8240−8252 Read Online

ACCESS | Metrics & More | Article Recommendations | Supporting Information

ABSTRACT: We report the aqueous lyotropic mesophase behaviors of protonated amine-based "lipidoids," a class of synthetic lipid-like molecules that mirrors essential structural features of the multitail bacterial amphiphile lipid A. Small-angle X-ray scattering (SAXS) studies demonstrate that the protonation of the tetra(amine) headgroups of six-tail lipidoids in aqueous HCl, HNO_3, H_2SO_4, and H_3PO_4 solutions variably drives their self-assembly into lamellar (L_α) and inverse micellar (I_{II}) lyotropic liquid crystals (LLCs), depending on acid identity and concentration, amphiphile tail length, and temperature. Lipidoid assemblies formed in H_2SO_4(aq) exhibit rare inverse body-centered cubic (BCC) and inverse face-centered cubic (FCC) micellar morphologies, the latter of which unexpectedly coexists with zero mean curvature L_α phases. Complementary atomistic molecular dynamics (MD) simulations furnish detailed insights into this unusual self-assembly behavior. The unique aqueous lyotropic mesophase behaviors of ammonium lipidoids originate in their dichotomous ability to adopt both inverse conical and chain-extended molecular conformations depending on the number of counterions and their identity, which lead to coexisting supramolecular assemblies with remarkably different mean interfacial curvatures.

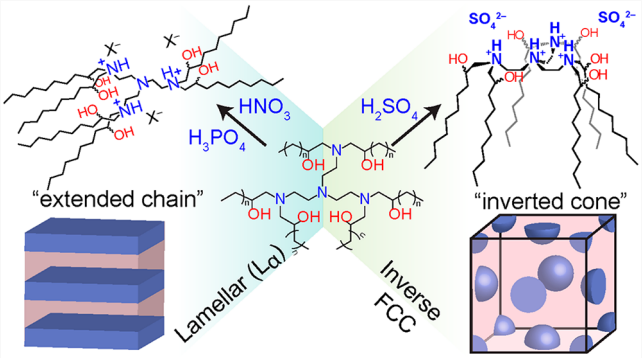

■ INTRODUCTION

Synthetic molecules inspired by the chemical structures and functions of biological amphiphiles are useful building blocks for the fabrication of new soft materials.[1−8] The self-assembly behaviors of cell membrane lipids have stimulated the design of synthetic materials and functional interfaces that exhibit supramolecular structures, physicochemical properties, and material functions that can exceed those of natural systems.[9−16] Although synthetic mimics of ubiquitous glycolipids and double-tailed phospholipids have been reported in this context,[2] little attention has focused on synthetic analogues of naturally occurring lipids bearing three or more hydrophobic tails.[4,6,8,17,18] Multitail structures potentially offer access to unique self-assembly behaviors and rare morphologies.[16,19,20] While synthetic approaches to multitail "lipidoids" with well-defined headgroup identities, tail lengths, and other key features have been previously reported,[21,22] the self-assembly behaviors of these pure compounds have not been extensively studied. A deeper understanding of the relationship between lipid structure and phase behavior will potentially enable the design of new functional materials based on biomimetic amphiphiles.

Lyotropic liquid crystals (LLCs) are functional supramolecular materials that spontaneously arise from amphiphile self-assembly in aqueous media.[16,23] LLC morphologies offer subtle insights into the curvature preferences of the underlying lipids, which often relate to their specific biological functions.[24,25] The LLC phase behaviors of amphiphiles depend strongly on their hydrated molecular shapes, which drive the formation of lamellar (L_α), bicontinuous network (Q), hexagonally packed cylinder (H), and discontinuous micellar (I) phases.[16,19,20,26,27] Assemblies that exhibit positive mean hydrophilic/hydrophobic interfacial curvature with a hydrophilic matrix phase are designated as type I or "normal" phases, whereas type II or "inverse" LLCs exhibit negative mean curvatures with hydrophobic matrices.[20] The lyotropic phase behaviors of synthetic surfactants are sometimes known to mimic the biological functions of their natural analogues. For example, synthetic gemini (twin head−twin tail) amphiphiles preferentially form negative Gaussian (saddle) curvature Q-phase LLC morphologies,[28−30] whereas double-

Received: May 8, 2020
Revised: June 24, 2020
Published: July 10, 2020

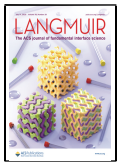

https://dx.doi.org/10.1021/acs.langmuir.0c01369
Langmuir 2020, 36, 8240−8252

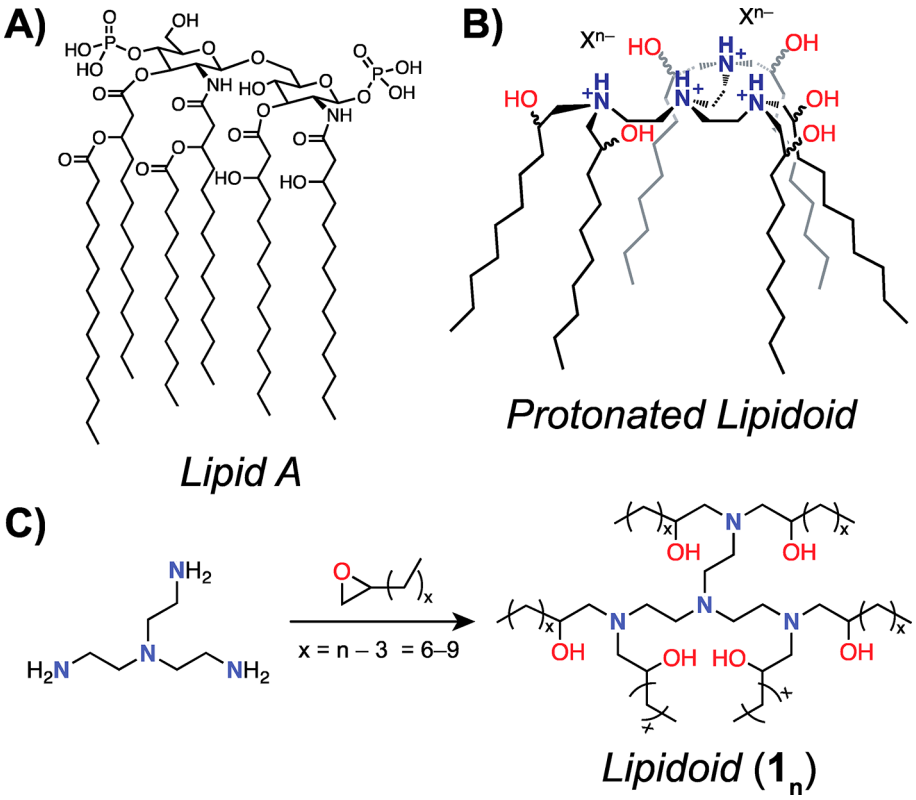

Figure 1. (A) Structure of a representative lipid A homologue comprising six tails and two phosphate headgroups from *E. coli*.[36] (B) Protonated six-tail lipidoids that undergo aqueous lyotropic self-assembly, derived from the acid treatment of (C) six-tail lipidoids ($\mathbf{1}_n$) that are readily obtained from a high yielding, one-step synthesis.

tailed surfactants typically enforce negative mean curvatures that can lead to ordered inverse micellar (I_{II}) phases.[31] The former discoveries in synthetic amphiphiles strikingly mirror the behavior of cardiolipin, a natural tetra-tail gemini lipid that promotes saddle curvature in bilayers, which is essential to cellular processes such as membrane pore formation and vesicle fusion/fission.[31−34]

Bacterial lipid A and its naturally occurring homologues (Figure 1A) display several desirable self-assembly characteristics,[35−38] which may be mimicked synthetically by lipidoids comprising multiple hydrophobic tails with pH-responsive headgroups. One key function of lipid A is to anchor lipopolysaccharides (LPS), also known as endotoxins, to the exterior surface of the outermost bilayer in Gram-negative bacteria. Although structural variations exist across species, lipid A typically bears at least six aliphatic tails and one or more phosphate-containing headgroups.[38,39] Studies of bacterial lipid A isolated from different species indicate that its homologues form various LLC phases, which depend on both their chemical structures and the surrounding aqueous environment.[35−38,40−46] The number and length of the lipid tails, in conjunction with the number and protonation state of the anionic phosphate headgroups, dictate the formation of I_{II}, inverse hexagonal (H_{II}), and L_α LLCs as functions of pH, temperature, and aqueous ionic strength.[35,36,41,42,45,47] The ability of lipid A to switch between morphologies with different transport properties in response to external stimuli could be a useful property for functional materials (e.g., from the connected water channels of a H_{II} phase to isolated water pools of I_{II} as a molecular "valve"). However, its inherent toxicity, hydrolytic instability, species-to-species variability, and low yields of isolated lipid necessitate the design of new synthetic analogues.

Herein, we report the protonation-driven self-assembly of a homologous series of six-tailed amphiphiles (Figure 1B,C) under a range of pH and temperature conditions, and we show that these multitail lipidoids mimic many key behaviors of bacterial lipid A. We previously reported that selected lipidoids trigger optical transitions in thermotropic liquid crystal microdroplets in a manner analogous to that for lipid A.[48,49] We speculated that this behavior arose from supramolecular self-assembly of the amphiphile and subsequent interactions with topological defects of the droplets. Using temperature-dependent synchrotron small-angle X-ray scattering (SAXS), we now show that the lyotropic self-assembly of six-tail lipidoids in acidic media depends sensitively on the tail length, temperature, headgroup protonation state, and counterion identity. Lipidoids with nine-carbon alkyl tails form a rare lyotropic body-centered cubic (BCC) packing of inverse spherical micelles. Lipidoids with longer tail lengths instead self-assemble into rare face-centered-cubic (FCC) packings of inverse micelles that coexist with zero mean curvature L_α phases. Atomistic molecular dynamics (MD) simulations of these self-assembly processes reveal that the occurrence of coexisting phases with starkly different interfacial curvatures originates in the unique ability of lipidoids to adopt both inverse conical and chain-extended amphiphile conformations on hydration. Establishing fundamental relationships between amphiphile structural features and their self-assembled LLC morphologies will open the door to new lipidoid applications in dynamic molecular transport and small-molecule delivery.

https://dx.doi.org/10.1021/acs.langmuir.0c01369
Langmuir 2020, 36, 8240−8252

■ EXPERIMENTAL SECTION

Materials. Tris(2-aminoethyl)amine (TREN, 96%) and *m*-chloroperoxybenzoic acid (*m*-CPBA, 70−75%) were purchased from Acros Organics (Morris Plains, NJ). 1,2-Epoxyoctane (99%), 1,2-epoxydecane (97%), 1,2-epoxydodecane (95%), and 1-undecene (97%) were purchased from Alfa Aesar (Radnor, PA). 1-Nonene was purchased from TCI America (Philadelphia, PA). 1-Iododecane (98%), Cs_2CO_3 (99%), concentrated H_2SO_4 (ACS grade, 95−98 wt %), concentrated HCl (ACS grade 37 wt %), concentrated HNO_3 (70 wt %), concentrated H_3PO_4 (85 wt %), CH_2Cl_2 (HPLC grade, >99.8%), $CHCl_3$ (HPLC grade, >99.8%), aqueous NH_4OH solution (ACS grade, 28−30 wt %), $CDCl_3$ (99.8% D), and dodecane (≥99%) were purchased from Sigma-Aldrich Chemical Co. (Milwaukee, WI). Diethyl ether was purchased from VWR (Radnor, PA). Methanol (MeOH; ACS grade) was purchased from Avantor Performance Materials (Center Valley, PA). SilicaFlash P60 silica gel (230−400 mesh) was purchased from Silicycle (Quebec City, QC). Anhydrous THF was obtained from a Pure Process Technology solvent purification system (Nashua, NH). Deionized water (18.2 MΩ·cm) was obtained from a Milli-Q system (Millipore, Bedford, MA) and is hereafter referred to as Milli-Q water. Silica gel TLC plates were purchased from Sigma-Aldrich (Milwaukee, WI), and compounds were visualized using I_2(s) vapor and an anisaldehyde-based stain. Unless otherwise noted, materials were used as received without further purification.

Molecular Characterization. ^{1}H and ^{13}C NMR spectra were recorded at 22 °C on either a Bruker Avance III 500 or a Varian INOVA 500 spectrometer. NMR chemical shift values were referenced to the residual proton or carbon peaks of $CDCl_3$ (δ 7.26 ppm for ^{1}H NMR spectra and δ 77.2 ppm for ^{13}C NMR). Sonication was performed using a Branson 2510 water bath sonicator operating at 22 °C. Mass spectrometry was performed on a Waters LCT electrospray ionization time-of-flight mass spectrometer using 10 mM NH_4OAc in CH_3CN or MeOH at a flow rate of 40 μL/min. Elemental analyses (C, H, and N) were conducted at Atlantic Microlab, Inc. (Norcross, GA, USA).

Synthesis of Odd-Carbon-Number 1,2-Epoxyalkanes. 1,2-Epoxyalkanes of 1-nonene and 1-undecene were synthesized by the following modification of a literature procedure.[50] The alkene (∼110 mM, 1.0 equiv) was dissolved in CH_2Cl_2 (300 mL) in a 500 mL round-bottom flask, which was immersed in an ice/H_2O bath. Solid *m*-CPBA (1.25 equiv) was added portionwise over ∼1 h. After the reaction was warmed to 22 °C, the solution was stirred overnight. The resulting clear solution was then concentrated to approximately half of its original volume under reduced pressure, transferred to a separatory funnel, and washed sequentially with saturated $NaHCO_3$(aq) (3 × 40 mL), 10 wt % NaOH(aq) (1 × 40 mL), and saturated NaCl(aq) (3 × 40 mL). The colorless organic phase was dried over Na_2SO_4(s) and gravity filtered through Whatman no. 2 filter paper, and the solvent was removed from the filtrate under reduced pressure to afford the desired product as a clear, colorless oil. 1,2-Epoxynonane: ^{1}H NMR (500 MHz, $CDCl_3$, 22 °C) δ (ppm) 0.88 (t, 3H), 1.28 (m, 8H), 1.39−1.56 (m, 4H), 2.46 (m, 1H), 2.74 (m, 1H), 2.90 (m, 1H). 1,2-Epoxyundecane: ^{1}H NMR (500 MHz, $CDCl_3$, 22 °C) δ (ppm) 0.88 (t, 3H), 1.26 (m, 12H), 1.38−1.56 (m, 4H), 2.46 (m, 1H), 2.74 (m, 1H), 2.90 (m, 1H).

Representative Synthesis of Six-Tail Lipidoids. Lipidoids are designated as $\mathbf{1}_n$, where n refers to the carbon number of the 1,2-epoxyalkane from which they originate (Figure 1C). Lipidoids $\mathbf{1}_{10}$ and $\mathbf{1}_{12}$ were synthesized and purified as previously described,[49] and $\mathbf{1}_9$ and $\mathbf{1}_{11}$ were analogously obtained by the ring-opening reaction of the desired 1,2-epoxyalkane with TREN. Briefly, TREN (1.0 equiv) and the desired 1,2-epoxyalkane (6.6 equiv) were weighed into a 6 mL glass vial, which was sealed and stirred at 90 °C for 4 days. Purification of the resulting reaction mixture by gradient elution flash chromatography [100% CH_2Cl_2 to 75:22:3 vol % CH_2Cl_2/MeOH/NH_4OH(aq)] furnished the desired products, typically in greater than 90% yield.

$\mathbf{1}_9$: ^{1}H NMR (500 MHz, $CDCl_3$, 22 °C) δ (ppm) 0.9 (t, −CH_3, 18H), 1.2−1.6 (m, −CH_2−72H), 2.2−3.0 (m, −N−CH−, 24H), 3.5−3.7 (m, −CH−OH, 6H), 5.0 (s, −OH, 6H). ^{13}C NMR (125.74 MHz, $CDCl_3$,22 °C) δ (ppm) 14.22, 22.80, 25.94 (m), 29.69, 30.11, 32.08, 35.17 (m), 62.76 (m), 64.44 (m), 67.63 (m), 70.01 (m). Elemental analysis: $C_{60}H_{126}N_4O_6$. Calcd: C, 72.1; H, 12.7; N, 5.6. Found: C, 71.1; H, 12.5; N, 5.6. Mass spectrometry (ESI+) m/z: Calcd $[M + H]^+$ 1000.7 g/mol, found 1000.0 g/mol.

$\mathbf{1}_{11}$: ^{1}H NMR (500 MHz, $CDCl_3$, 22 °C) δ (ppm) 0.9 (t, −CH_3, 18H), 1.2−1.6 (m, −CH_2− 96H), 2.2−3.0 (m, −N−CH−, 24H), 3.5−3.7 (m, −CH−OH, 6H), 5.0 (s, −OH, 6H). ^{13}C NMR (125.74 MHz, $CDCl_3$,22 °C) δ (ppm) 14.24, 22.85, 25.88 (m), 29.03, 29.32, 29.88 (m), 32.57, 33.93, 35.06 (m), 62.64 (m), 64.62 (m), 67.74 (m), 70.08 (m). Elemental analysis: $C_{72}H_{150}N_4O_6$. Calcd: C, 74.0; H, 13.0; N, 4.8. Found: C, 74.2; H, 13.1; N, 4.9. Mass spectrometry (ESI+) m/z: Calcd $[M + H]^+$ 1169.0 g/mol, found 1168.2 g/mol.

Preparation of Lipidoid LLCs in Acidic Aqueous Media. Lipidoids (∼20 mg) were weighed into 24 mL glass vials, and 15 mL of acidic solution was added to yield a final lipidoid concentration of 0.133 wt % (1.06−1.33 mM in solution). While the CMCs for these lipidoids were not directly determined, our previous study suggests that they aggregate even at picomolar concentrations.[49] The acidic solution ionic strength was set to I = 6 M, which was calculated from $I = \frac{1}{2}n\sum_{i=1}^{i=n} c_i z_i^2$, where n is the number of ions in solution and c_i and z_i are the respective concentrations (in mols/dm^3) and charges of species i. The resulting dispersions were vortex mixed for 30 s, sonicated in a water bath for 30 s, and then quiescently annealed at 90 °C in an oil bath for 2 h. After cooling to 22 °C, the physical consistencies of the lipidoids in acidic dispersions ranged from viscous oils to stiff, solid-like materials in excess solution. These LLCs were subsequently handled in the presence of excess liquid to ensure preservation of the LLC morphology since the amphiphile protonation reaction is an equilibrium process.

To prepare oil-swollen samples, a mixture of $\mathbf{1}_{10}$ (5 mg) and dodecane (14 mg) was dissolved in diethyl ether (200 mg). This solution was added dropwise to 3 M H_2SO_4(aq) (3.75 mL), and the ether was allowed to evaporate over 1 h at 22 °C to yield a solid-like disc at the surface of the acidic solution. As a control experiment, $\mathbf{1}_{10}$ (5 mg) was dissolved in ether and a sample was prepared as above in the absence of oil.

Composition Analyses of Protonated Lipidoids. Excess acid solution was decanted to isolate the protonated lipidoid LLC, which was then transferred to a tared sample vial. The vial was centrifuged at 4000 rpm for 5 min to promote the expulsion of any excess aqueous solution, which was absorbed and removed from the vial using a Kimwipe. This process was carried out four times or until a constant LLC mass (m_{LLC}) was achieved. The LLC was then frozen in N_2(l) and dried under high vacuum at 22 °C for 48 h, prior to further drying to a constant mass (m_{dry}) under high vacuum at ∼80 °C. The water mass (m_{water}) was calculated as $m_{water} = m_{LLC} - m_{dry}$, assuming that the mass loss under vacuum stemmed solely from water evaporation. Elemental analysis (C, H, N) was performed on these dry samples to calculate the number of acid molecules per lipidoid and thus estimate the tetra(amine) headgroup protonation state as follows. The theoretical CHN content of a lipidoid coordinated with various molar quantities of acid were calculated (Table 1) and matched to the experimentally observed CHN composition. For example, elemental

Table 1. Acid Composition Estimate for the LLC Formed by Lipidoid $\mathbf{1}_{10}$ in 1 M H_2SO_4(aq) Based on the Elemental Analysis of a Dried LLC Isolate

$[H_2SO_4]/[\mathbf{1}_{10}]$	theoretical formula	C	H	N
1.8	$C_{66}H_{141.6}N_4O_{13.2}S_{1.8}$	62.90	11.32	4.45
1.9	$C_{66}H_{141.8}N_4O_{13.6}S_{1.9}$	62.41	11.25	4.41
2.0	$\mathbf{C_{66}H_{142}N_4O_{14}S_2}$	**61.93**	**11.18**	**4.38**
2.1	$C_{66}H_{142.2}N_4O_{14.4}S_{2.1}$	61.46	11.11	4.34
2.2	$C_{66}H_{142.4}N_4O_{14.8}S_{2.2}$	61.00	11.04	4.31

https://dx.doi.org/10.1021/acs.langmuir.0c01369
Langmuir 2020, 36, 8240−8252

analysis of the dried residue resulting from the $\mathbf{1}_{10}$ LLC formed in excess 1 M H_2SO_4(aq) yielded mass fractions of C 61.90%, H 11.23%, and N 4.28%. From Table 1, we find that the theoretical composition that most closely matches the experimental one (within the expected variance of ±0.4%) exhibits $[H_2SO_4]/[\mathbf{1}_{10}]$ = 2.0 with $[\mathbf{1}_{10}]$ = 1.06−1.33 mM. This composition suggests a fully protonated headgroup coordinated with two SO_4^{2-} counterions.

Small- and Wide-Angle X-ray Scattering (SAXS and WAXS) Analyses. Synchrotron SAXS analyses were conducted at the 12-ID-B beamline of the Advanced Photon Source (Argonne, IL, USA) using 14.00 keV (λ = 0.8856 Å) beam energy. Two-dimensional SAXS and WAXS patterns were collected on a Pilatus 2 M area detector (172 μm × 172 μm pixel size) with a sample-to-detector distance of either 2.000 or 3.616 m, as calibrated with a silver behenate standard (d = 58.38 Å). Lipidoid LLCs in their excess supernatant acidic media were sealed in quartz capillaries (Hampton Research) or Kapton tubes (Cole-Parmer) for analysis. Temperature-dependent SAXS analyses employed a heated multicapillary array stage on which samples were equilibrated at each temperature for at least 10 min prior to X-ray exposure for 0.1−1 s. Two-dimensional SAXS patterns were azimuthally integrated using the DataSqueeze software package (http://www.physics.upenn.edu/~heiney/datasqueeze/index.html) to obtain 1D-SAXS intensity $I(q)$ versus q (Å^{-1}) scattering profiles.

Lab source SAXS was conducted on a Bruker NANOSTAR instrument equipped with a microfocus Cu Kα X-ray source. X-rays were collimated using scatterless slits (Xenocs, France), and patterns were collected on a HiStar2D multiwire gas detector (Bruker-Siemens) calibrated with silver behenate to a 26 cm sample-to-detector distance. Two-dimensional SAXS patterns were processed into 1D-SAXS intensity profiles using *Nika* macros[51] for Igor Pro.

SAXS intensity and associated form factor analyses for LLCs formed by $\mathbf{1}_9$, $\mathbf{1}_{10}$, and $\mathbf{1}_{11}$ protonated with H_2SO_4(aq) employed the core−shell−shell model in the *Irena* macro[51] for Igor Pro. The neat lipidoid densities used in these fits were determined by recording the mass of 10 μL of lipidoid drawn up into a tared volumetric capillary (Accu-Glass, Valencia, CA).

Le Bail Refinement of Synchrotron SAXS Data. The *JANA2006* software package[52] was used to extract structure factor intensities associated with each peak in a given SAXS pattern and to determine the refined unit cell parameter.[53−55] Application of the charge-flipping algorithm implemented within the *SUPERFLIP*[56] software package to the extracted structure factor intensity data enabled the reconstruction of 3D electron density maps for each phase, which were visualized in the *VESTA* software environment.[57] Reported electron density maps represent averages of ≥50 separate charge-flipping algorithm convergences with figures of merit $fm \leq 10$.

Molecular Dynamics (MD) Simulations. Atomistic MD simulations of six-tail lipidoids were carried out in *GROMACS* version 4.6.5.[58] Force field parameters were largely based on the *GROMOS45a3* united atom force field[59] in which H atoms on the aliphatic carbon tails are not treated explicitly, while H atoms on the hydroxyl groups, HSO_4^- ions, and the protonated amines of the lipidoids are explicitly represented. Headgroup atom partial charges were fitted using the CHARMM general force field (*CGenFF*) program.[60] The partial charges for HSO_4^- counterions were taken from the work of Ishiyama and Morita,[61] and the SPC model[62] was used for water molecules.

LLC self-assembly simulations at microsecond time scales were carried out for $\mathbf{1}_9$ and $\mathbf{1}_{12}$ in 1 M H_2SO_4(aq) using the experimentally determined lipidoid/counterion/water ratios. The phase behaviors of $\mathbf{1}_{10}$ and $\mathbf{1}_{11}$ in 1 M H_2SO_4(aq) were not simulated due to the observed L_α/I_{II} phase coexistence. For simulations of LLC unit cells of $\mathbf{1}_9$ in 1 M H_2SO_4(aq), molecules were randomly placed in a cubic box (see Table S1 for details) and equilibrated in the NPT ensemble using the Berendsen barostat.[63] To ensure adequate equilibration, multiple sets of NVT simulations at T = 600 K with 100−500 ns durations were conducted prior to NPT simulations at 1 atm and the desired temperature. Following 60 ns of NPT equilibration, the self-assembled structure with a cubic unit cell size of a = 3.24 nm was then further relaxed in the NVT ensemble for 2 μs. For the simulation of the L_α phase of $\mathbf{1}_{12}$ in 1 M H_2SO_4(aq), initial self-assembly studies were performed in a cubic cell with an edge dimension of a = 2.9 nm (details in Table S1). The resulting L_α-like structure was then duplicated in the xy plane and equilibrated for 30 ns in the NPT ensemble at 1 atm and the desired temperature. Semi-isotropic pressure coupling was used to maintain the L_α phase. NVT simulation (500 ns) was then employed to obtain the final L_α structure at 350 K with a domain spacing of d = 2.69 nm, which is ∼8% smaller than the experimental value of 2.93 nm. Given unavoidable experimental LLC composition analysis uncertainties, an LLC with a 6.7% lower hydration level was prepared and simulated (Table S1). This system remained stable during 2 μs of NPT simulation, and the obtained lamellar spacing of d = 2.86 nm was in closer agreement with the experimental value. Thus, the lower hydration system was used for detailed structural analyses. Further details of the force field parametrization and simulation conditions are given in the Supporting Information.

■ RESULTS AND DISCUSSION

Lipidoids were synthesized by an established one-step, ring-opening reaction of tris(2-aminoethyl)amine (TREN) with 1,2-epoxynonane, 1,2-epoxydecane, 1,2-epoxyundecane or 1,2-epoxydodecane to produce $\mathbf{1}_9$, $\mathbf{1}_{10}$, $\mathbf{1}_{11}$, and $\mathbf{1}_{12}$, respectively (Figure 1C).[49] While prior reports on amphiphiles with polyamine headgroups and ≥3 tails have focused on their dilute solution self-assembly behaviors,[64−66] investigations of the LLC self-assembly of such lipids in concentrated solutions have yet to be reported. Pure lipidoids display no propensity for thermotropic liquid crystal self-assembly, and lipidoids dispersed in pure H_2O do not lyotropically self-assemble[49] due to a lack of incompatible chemical functionalities needed to drive segregation and ordering. However, we reasoned that protonation of the polybasic headgroup would drive segregation of the water-solvated ionic headgroups from the hydrophobic tails (Figure 1B) to induce self-assembly.

LLC Self-Assembly in Acidic Media. In a preliminary study, we reported that protonating $\mathbf{1}_{10}$ with 1 M H_2SO_4(aq) induced its self-assembly into a cubic LLC morphology that was tentatively assigned the space group symmetry $P4_232$ based on low-resolution SAXS data.[49] In order to unequivocally identify this LLC morphology and to elucidate how counterion identity guides lipidoid self-assembly, we systematically characterized LLCs formed by the protonation of $\mathbf{1}_n$ (n = 9−12) by aqueous HCl(aq), HNO_3(aq), and H_3PO_4(aq). Aqueous acid concentrations were set so that the solution ionic strength I = 6 M matched that of 1 M H_2SO_4(aq) used in our earlier study. We refer to protonated lipidoid LLC samples using the convention $\mathbf{1}_n$-x**A**, where n is the number of carbons in each tail and x denotes the acid **A** solution molarity, where **A** = **C**(HCl), **N**(HNO_3), **P**(H_3PO_4), and **S**(H_2SO_4). (See the Experimental Section for sample preparation details.)

Acid solution treatment of the lipidoids yielded variable results, ranging from the formation of viscous oils to stiff solids that persist in excess solution, depending on the acid identity and lipidoid tail length. We investigated the resulting materials morphologies using synchrotron SAXS and WAXS. $\mathbf{1}_n$-**3C** and $\mathbf{1}_n$-**3N** exhibited numerous sharp WAXS and SAXS peaks (Figures S1 and S2), which suggest significant molecular-level crystallinity that we attribute to crystalline, protonated lipidoids. However, the superposition of equally spaced SAXS peaks in X-ray patterns for $\mathbf{1}_n$-**3N** (n = 10−12) located at (q/q^*) = 1, 2,... (Figure S2) also implies the formation of coexisting L_α LLCs. Since surfactant crystallinity competes significantly with LLC mesophase formation, we abandoned

https://dx.doi.org/10.1021/acs.langmuir.0c01369
Langmuir 2020, 36, 8240−8252

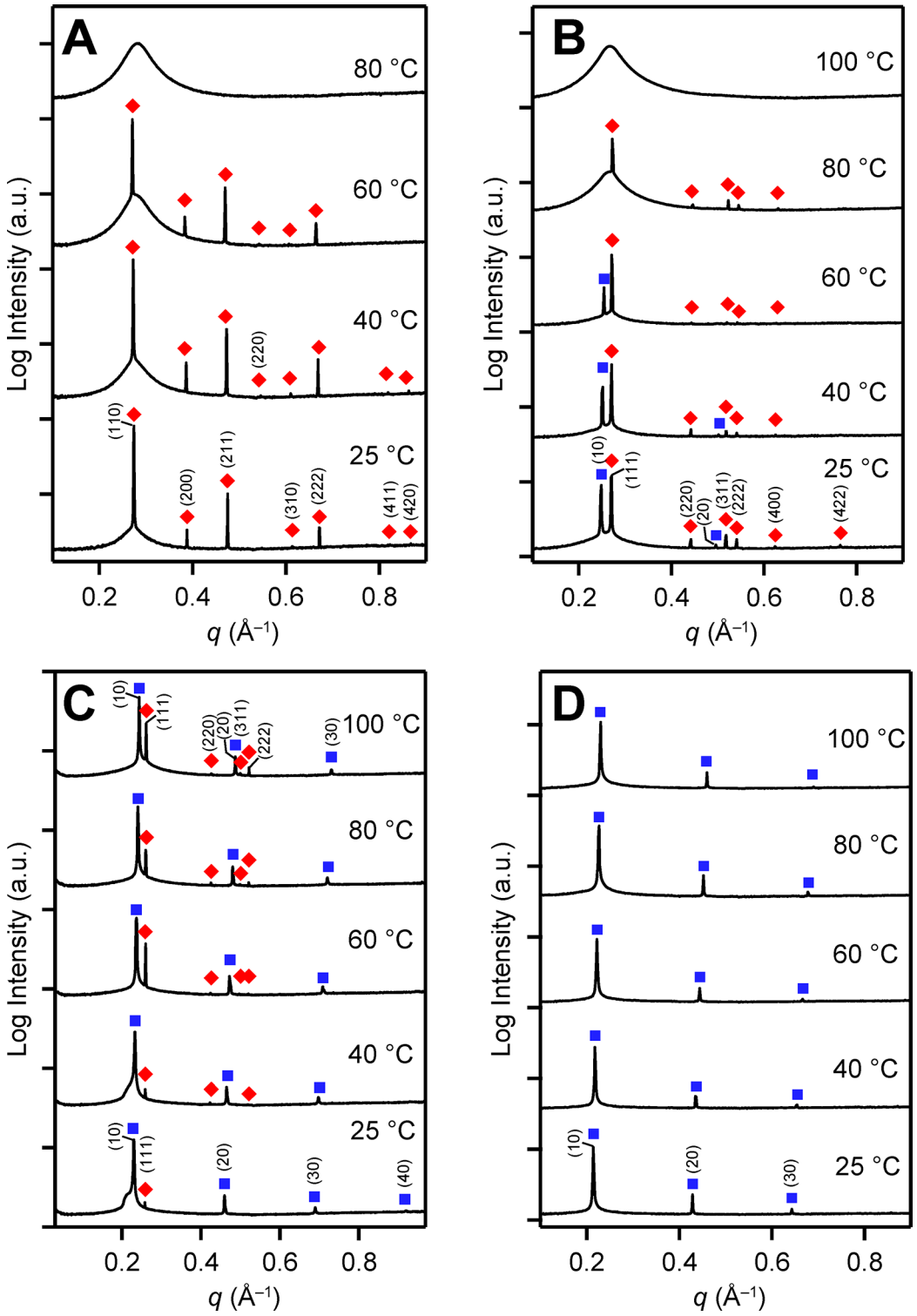

Figure 2. Temperature-dependent synchrotron SAXS data for LLCs: (A) $\mathbf{1_9}$**-1S**, (B) $\mathbf{1_{10}}$**-1S**, (C) $\mathbf{1_{11}}$**-1S**, and (D) $\mathbf{1_{12}}$**-1S** formed by lipidoid protonation in 1 M H_2SO_4(aq). Expected peak positions for L_α (blue squares) and I_{II} (red diamonds) phases are labeled, along with the corresponding Miller indices. The broad scattering features observed in $\mathbf{1_9}$**-1S** and $\mathbf{1_{10}}$**-1S** at elevated temperatures are signatures of disordered phases, which sometimes coexist with an ordered LLC.

detailed studies of $\mathbf{1}_n$**-*x*C** and $\mathbf{1}_n$**-*x*N**. Changing the protonation medium to 0.5 M H_3PO_4(aq) with I = 6 M drives LLC formation absent any signs of protonated lipidoid crystallinity, given the featureless WAXS patterns for these samples (Figure S3). SAXS analyses of $\mathbf{1}_n$**-0.5P** (n = 10−12) reveal sharp scattering maxima at (q/q^*) = 1 and 2 (Figure S3) that are consistent with L_α LLCs with domain spacings of d = 2.47−2.91 nm, which monotonically increase with n. For $\mathbf{1_{10}}$**-0.5P** and $\mathbf{1_{11}}$**-0.5P** LLCs, SAXS patterns also exhibit a broad scattering feature superposed on the sharp SAXS peaks that indicates phase coexistence with a disordered state. Note that $\mathbf{1_9}$**-3N** and $\mathbf{1_9}$**-0.5P** apparently form only disorganized phases

https://dx.doi.org/10.1021/acs.langmuir.0c01369
Langmuir 2020, 36, 8240−8252

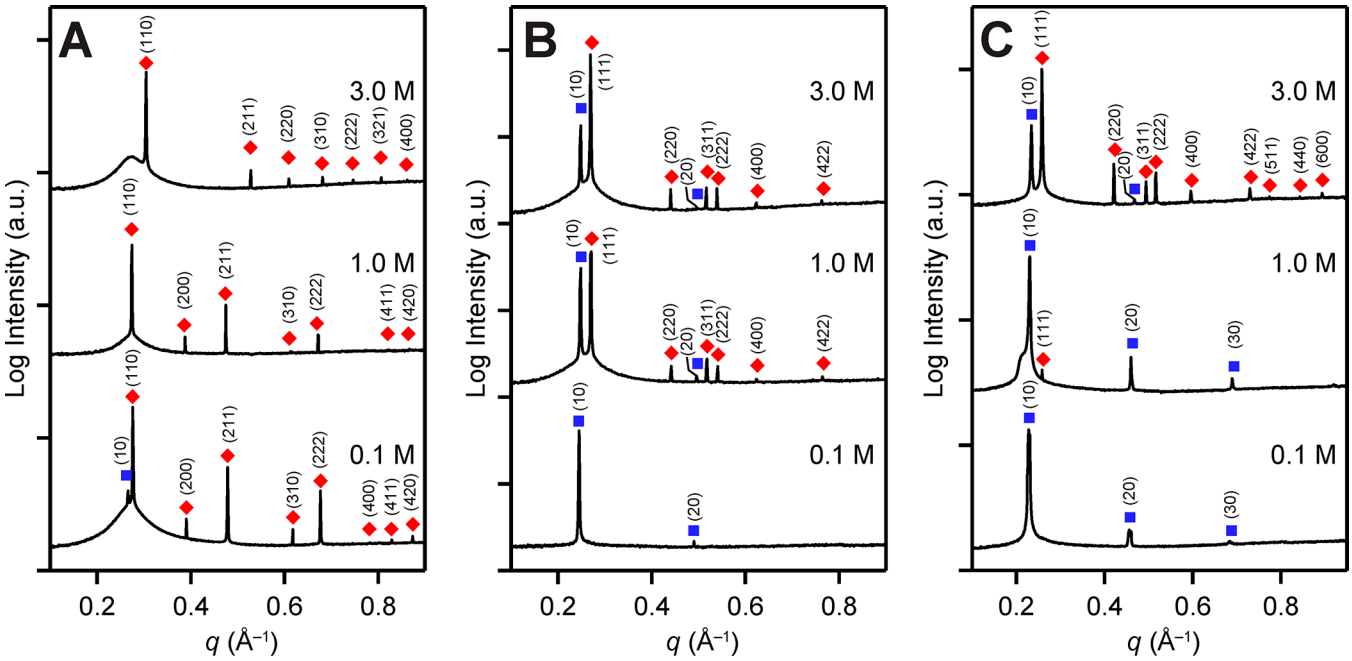

Figure 3. Synchrotron SAXS data obtained at 25 °C for lipidoids LLCs derived from (A) $\mathbf{1_9}$, (B) $\mathbf{1_{10}}$, and (C) $\mathbf{1_{11}}$ protonated with the labeled H_2SO_4(aq) concentrations. Expected peak positions for L_α (blue squares) and cubic (red diamonds) phases are marked with the associated Miller indices. The broad scattering feature observed in all $\mathbf{1_9}$ samples arises from the two-phase coexistence of ordered and disordered states.

with a single correlation peak and no higher-order SAXS maxima (Figures S2−S3). These results contrast starkly with the rich LLC phase behaviors of lipidoids protonated with 1 M H_2SO_4(aq), as evidenced by the complex temperature-dependent SAXS patterns obtained for $\mathbf{1_n}$**-1S** with n = 9−12 (Figure 2) and the absence of any WAXS peaks with $q \geq 1.0$ Å^{-1} (Figure S4). Consequently, we focused on understanding the impact of the tail length, temperature, and acid concentration on the phase behavior of $\mathbf{1_n}$-x**S** samples.

Tail Length and Temperature-Dependent Self-Assembly of $\mathbf{1_n}$-1S. SAXS patterns for $\mathbf{1_9}$**-1S** (Figure 2A) exhibit Bragg peaks with scattering wavevector ratios of q/q^* = $\sqrt{2}$, $\sqrt{4}$, $\sqrt{6}$, $\sqrt{10}$, $\sqrt{12}$, $\sqrt{18}$, and $\sqrt{20}$ (q^* = 0.195 Å^{-1}) consistent with cubic space group symmetry. These scattering maxima are consistent with the (110), (200), (211), (310), (222), (411), and (420) reflections of a BCC structure ($Im\bar{3}m$ symmetry) with lattice parameter a = 3.22 nm or the (100), (110), (111), (210), (211), (300), and (310) reflections of a simple cubic (SC) lattice ($Pm\bar{3}m$ symmetry) with a unit cell dimension of a = 2.28 nm. In the absence of additional data, we prefer the higher space group symmetry per crystallographic convention. Upon heating this sample to 40 °C, an additional peak appears at q/q^* = $\sqrt{8}$, consistent with the (220) reflection of the putative BCC unit cell. We further observe an order-to-disorder transition at 80 °C at which the sharp Bragg peaks disappear, leaving a single, broad peak corresponding to a disordered-state correlation length. The observation of an inverse BCC LLC supports our hypothesis that six-tail ammonium lipidoids exhibit biomimetic phase behaviors, given that Reichelt et al. previously reported that lipid A also self-assembles into an inverse BCC phase in NaCl(aq).[42] While the SAXS data resolution in this last report is relatively low with only four observed SAXS peaks, the higher-resolution data presented here furnish a higher degree of confidence in the assigned inverse BCC phase (vide infra).

In our earlier report, we had tentatively assigned the LLC formed by $\mathbf{1_{10}}$**-1S** as a low-symmetry, cubic structure based on low-resolution SAXS analyses.[49] However, high-resolution synchrotron SAXS patterns acquired from this sample at 25 °C (Figure 2B) indicate that the observed peaks do not originate from a single LLC phase. The first scattering peak located at q_L^* = 0.248 Å^{-1} and the peak at $2q_L^*$ correspond to an L_α phase with a domain spacing of d = 2.53 nm, which is comparable to that of the $\mathbf{1_{10}}$**-0.5P** L_α phase. An analysis of the remaining peaks in this pattern reveals that they occur at q/q_c^* = $\sqrt{3}$, $\sqrt{8}$, $\sqrt{11}$, $\sqrt{12}$, $\sqrt{16}$, and $\sqrt{24}$ (q_c^* = 0.156 Å^{-1}) that correspond to the (111), (220), (311), (222), (400), and (422) reflections of a cubic structure with lattice constant a = 4.03 nm. On the basis of these SAXS peak positions, this phase exhibits either $Fm\bar{3}m$ or $Fd\bar{3}m$ symmetry. Upon heating this sample to 80 °C, the L_α peaks diminish in intensity and disappear, leaving behind only the face-centered lattice scattering peaks at q/q_c^* = $\sqrt{3}$, $\sqrt{8}$, $\sqrt{11}$, $\sqrt{12}$, and $\sqrt{16}$ (q_c^* = 0.157 Å^{-1}) with a broad underlying scattering feature at ∼0.25 Å^{-1} of a disordered phase. This unusual L_α/cubic two-phase coexistence was confirmed by polarized optical microscopy, wherein we observed a mixture of birefringent (L_α) and nonbirefringent (cubic) regions in $\mathbf{1_{10}}$**-1S** at 22 °C. Note that heating $\mathbf{1_{10}}$**-1S** to 100 °C drives the melting of the cubic LLC to yield a fully disordered fluid. SAXS patterns for this ordered face-centered-cubic LLC strongly resemble the lower-resolution data previously reported by Reichelt et al. for lipid A assembled in NaCl(aq),[42] including the notable absence of a (200) reflection with q/q_c^* = $\sqrt{4}$. Again, these data demonstrate the biomimetic self-assembly characteristics of the $\mathbf{1_n}$ lipidoids.

Incrementing the lipidoid tail length as in $\mathbf{1_{11}}$**-1S** led to a somewhat surprising change in the observed LLC morphologies. SAXS analysis of $\mathbf{1_{11}}$**-1S** at 22 °C revealed a series of sharp and equally spaced Bragg peaks indicative of an L_α phase with an interlayer spacing of d = 2.74 nm, alongside a broad

https://dx.doi.org/10.1021/acs.langmuir.0c01369
Langmuir 2020, 36, 8240−8252

scattering maximum near q^* and a sharp peak at a slightly higher q value (Figure 2C). Upon heating this sample, the intensity of the sharp peak increased concomitantly with the appearance of ≥4 SAXS peaks that do not correspond to an L_α phase. This two-phase coexistence persists up to 100 °C, at which the new peaks exhibit $q/q_c^* = \sqrt{3}$, $\sqrt{8}$, $\sqrt{11}$, and $\sqrt{12}$ ($q_c^* = 0.151$ Å^{-1}) which again correspond to either $Fm\bar{3}m$ or $Fd\bar{3}m$ cubic phases with a lattice constant of $a = 4.16$ nm. In sharp contrast, $\mathbf{1_{12}}$**-1S** forms only L_α LLCs with $d = 2.93$ nm ($q^* = 0.214$ Å^{-1}) at 25 °C (Figure 2D). These lamellae remain thermally stable up to 100 °C, with a d spacing that decreases slightly at higher temperatures, with no evidence of cubic phase formation.

Thus, protonating the homologous lipidoid series $\mathbf{1_9}$−$\mathbf{1_{12}}$ with 1 M H_2SO_4(aq) drives the phase progression of cubic → cubic + L_α → L_α with increasing tail length and decreasing temperature. In all cases, the samples recover their as-made LLC morphologies on thermal cycling between 22 and 100 °C. The last observation suggests equilibrium structure formation under our lipidoid protonation protocol, including instances of two-phase coexistence, which are thermodynamically anticipated by Gibbs' phase rule. However, the exact symmetry and topology of the cubic LLC morphology coexisting with the zero mean curvature L_α LLC remained uncertain on the basis of the SAXS data presented thus far. Curvature arguments lead one to expect that the BCC and FCC mesophases are polycontinuous networks since these negative Gaussian curvature morphologies are typically found in adjacent regions of phase space to zero-curvature L_α phases. Since we hypothesized that the polybasic tetra(amine) headgroup could impart pH-dependent self-assembly behaviors similar to that reported for bacterial lipid A,[36,37,41,45] we pursued this avenue of investigation toward more conclusive assignments of cubic LLC structures.

Acid-Strength-Dependent Self-Assembly of $\mathbf{1_n}$-*x*S. To understand the effects of solution pH on self-assembly, lipidoids $\mathbf{1_n}$ were protonated in 0.1 and 3 M H_2SO_4(aq) for comparison with the $\mathbf{1_n}$**-1S** samples (Figure 3). $\mathbf{1_9}$**-0.1S** yielded a 25 °C SAXS pattern with scattering maxima at $q/q^* = \sqrt{2}$, $\sqrt{4}$, $\sqrt{6}$, $\sqrt{10}$, $\sqrt{12}$, $\sqrt{16}$, $\sqrt{18}$, and $\sqrt{20}$ ($q^* = 0.195$ Å^{-1}), which correspond to the (110), (200), (211), (310), (222), (400), (411), and (420) reflections of a BCC structure with $a = 3.22$ nm, the same lattice parameter found for $\mathbf{1_9}$**-1S**. However, the low-intensity peak at $q = 0.266$ Å^{-1} suggests the formation of a small amount of L_α LLC with a spacing of $d = 2.36$ nm. This last assignment is tentative given the absence of higher-order lamellar SAXS peaks. At the highest acid concentration, $\mathbf{1_9}$**-3S** exhibits SAXS peaks at $q/q_c^* = \sqrt{2}$, $\sqrt{6}$, $\sqrt{8}$, $\sqrt{10}$, $\sqrt{12}$, $\sqrt{14}$, $\sqrt{16}$, and $\sqrt{18}$, consistent with the (110), (211), (220), (310), (222), (321), (400), (411), and (420) reflections of a BCC unit cell with $a = 2.91$ nm (top trace in Figure 3A). The notable presence of the (321) peak enables the unequivocal assignment of this phase as a BCC structure with $Im\bar{3}m$ symmetry because this peak is forbidden in the aforementioned $Pm\bar{3}m$ symmetry. Note that the (200) peak is not observed in this SAXS pattern, likely because of form factor scattering extinction due to the specific sizes of the hydrophilic and hydrophobic domains (vide infra). In each of the $\mathbf{1_9}$-*x*S LLCs, a broad scattering feature is observed under the sharp Bragg peaks that indicates the coexistence of ordered LLCs with disordered states. $\mathbf{1_{10}}$**-0.1S** and $\mathbf{1_{11}}$**-0.1S** form L_α phases with respective interlayer spacings of $d = 2.57$ and 2.76 nm (Figure 3B,C), consistent with values obtained on their protonation with 1 M H_2SO_4(aq). Protonation with 3 M H_2SO_4(aq) as in $\mathbf{1_{10}}$**-3S** and $\mathbf{1_{11}}$**-3S** again drives the formation of L_α/cubic phase coexistence with cubic lattice parameters similar to those of $\mathbf{1_{10}}$**-1S**, and $\mathbf{1_{11}}$**-1S** at elevated temperatures. While the conspicuous absence of the (200) peak suggests that the latter patterns conform to the $Fd\bar{3}m$ space group per the work of Reichelt et al.,[42] the (600) reflection is not allowed by this space group symmetry. Thus, observation of the (600) reflection in the SAXS pattern of $\mathbf{1_{11}}$**-3S** unequivocally demonstrates that the cubic phase that coexists with L_α has $Fm\bar{3}m$ symmetry. Finally, we observed primarily L_α LLCs for $\mathbf{1_{12}}$ at all studied acid concentrations (data not shown). In summary, the overall propensity for inverse BCC or FCC phase formation increases with increasing H_2SO_4 concentration at the expense of the L_α phases on protonating $\mathbf{1_n}$ with $n = 9$−11.

Structure Determination by Electron Density Reconstruction. Given the unusual nature of the $Fm\bar{3}m$/L_α LLC two-phase coexistence observed in $\mathbf{1_{10}}$**-1S** and $\mathbf{1_{11}}$**-3S**, we sought to elucidate the structures of the cubic LLCs by reconstructing electron density maps for each of these phases. We specifically aimed to assess whether the BCC and FCC structures were discontinuous micellar or polycontinuous network phases, the latter of which exhibit negative Gaussian curvatures at mean curvatures close to zero that may coexist with L_α. We note that Reichelt et al. previously obtained a SAXS pattern from a lipid A LLC that closely resembles the one for $\mathbf{1_9}$**-1S**. While these authors assigned this phase to inverse BCC micelle packing, they presented scant evidence for the discontinuous micellar nature of this LLC.[42] In order to resolve this quandary, we selected SAXS patterns from $\mathbf{1_9}$-*x***S** (x = 0.1, 1, and 3) and $\mathbf{1_n}$-*x***S** (n = 10 or 11, x = 1 or 3) with the largest number of SAXS peaks for detailed analysis.

Using the *JANA2006* crystallographic computing software,[52] we performed a Le Bail refinement of the SAXS pattern for $\mathbf{1_9}$**-1S** at 25 °C after thermal cycling above 40 °C to extract X-ray structure factor intensities associated with the sharp peaks at $(q/q^*)^2$ = 2, 4, 6, 8, 10, 12, 18, 20, and 24 (Figure S5). Given the structural homology of this LLC phase to that obtained from $\mathbf{1_9}$**-3S** that unambiguously exhibits BCC symmetry, we used the $Im\bar{3}m$ symmetry to obtain a refined lattice parameter of $a = 3.24$ nm. Application of the charge-flipping algorithm implemented in the *SUPERFLIP* software package[56] to these structure factor intensities enabled reconstruction of an electron density map for this phase (Figure 4A). This map shows that $\mathbf{1_9}$**-1S** comprises a BCC packing of discontinuous

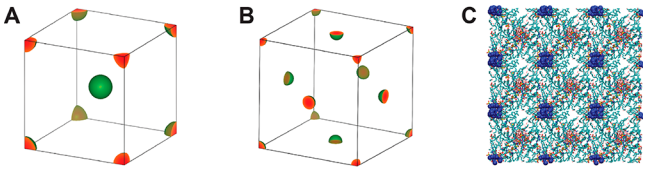

Figure 4. Electron density maps (90% isosurfaces) for (A) the inverse BCC phase ($Im\bar{3}m$ symmetry) formed by $\mathbf{1_9}$**-1S** at 25 °C with a lattice parameter of $a = 3.22$ nm and (B) the inverse FCC phase ($Fm\bar{3}m$ symmetry) formed by $\mathbf{1_{11}}$**-3S** at 25 °C, in each of which the green spheres with orange cores represent water-rich nanodomains. (C) Snapshot of the BCC structure obtained from a bias-free MD simulation for $\mathbf{1_9}$**-1S**, in which blue and pink spheres represent the atoms in water molecules and the polyamine headgroups within 5 Å of the BCC lattice sites and the cyan lines represent the lipidoid tails.

https://dx.doi.org/10.1021/acs.langmuir.0c01369
Langmuir 2020, 36, 8240−8252

spherical micelles of identical volumes. Given the persistence of $\mathbf{1_9}$-**1S** LLCs in excess acid solution, we conclude that this phase is an inverse LLC in which isolated acidic water nanopools are ordered in a hydrophobic matrix. To the best of our knowledge, this phase represents the first definitive report of an inverse micellar BCC LLC in any small-molecule surfactant.

In our initial attempts to reconstruct an electron density map for the FCC structure, we used the SAXS pattern for the pure phase observed in $\mathbf{1_{10}}$-**1S** at 80 °C that does not exhibit L_α coexistence (Figure 2B). However, this approach was fraught with problems since this pattern exhibits only five SAXS peaks along with interference from a broad feature of a disordered phase. Consequently, we conducted a Le Bail refinement of the SAXS pattern for $\mathbf{1_{11}}$-**3S** at 25 °C in Figure 3C with $Fm\bar{3}m$ symmetry, from which we omitted the L_α peaks to obtain the desired structure factor intensities with a refined lattice constant of a = 4.22 nm (Figure S6). The electron density map obtained by application of the *SUPERFLIP* charge-flipping algorithm to these Fourier amplitudes reveals an FCC micelle packing (Figure 4B). The persistence of this LLC in excess acidic water again implies the formation of an inverse FCC phase. The first example of such a phase was only recently reported by Mezzenga and co-workers.[67,68] Thus, the FCC phases of $\mathbf{1_{11}}$-**3S** and $\mathbf{1_{10}}$-**1S** comprising acidic water nanopools ordered in a hydrophobic matrix represent only the second such example of this supramolecular structure in aqueous LLCs.

We note that a structurally related, inverse hexagonally closest-packed (HCP) LLC with a high degree of long-range translational order was previously reported by Shearman et al. in binary lipid mixtures under large hydrostatic pressures.[69] This HCP phase exhibits alternating ABABAB... packing of hexagonally closest-packed A and B layers of spherical micelles, whereas the FCC phase reported here exhibits ABCABC... close-packed micelle layer stacking. Thus, the FCC and HCP phases are related by stacking faults.[70] The fact that we find an inverse FCC structure with no stray SAXS peaks is striking, in view of recent results by Jayaraman et al.[71] who observed a defect-ridden normal FCC phase with stacking faults corresponding to local HCP-like order in a nonionic surfactant LLC. It is currently unclear what the underlying driving force is for the preferential formation of FCC versus HCP phases in lipidic LLCs given their crystallographic relationship through martensitic shear transformations recently described by Lee and co-workers.[72] Nonetheless, the multitail lipidoid structure apparently stabilizes inverse micellar cubic LLCs inaccessible in simpler lipid−water mixtures.

The SAXS data for the inverse micellar $Fm\bar{3}m$ (FCC) phase in all cases exhibits a (200) reflection extinction, which we attribute to a form factor extinction due to the specific micelle dimensions and electron density distributions therein. We initially attempted to determine the micelle sizes by fitting the total scattering intensity in the SAXS patterns for $\mathbf{1_{10}}$-**1S** and $\mathbf{1_{11}}$-**3S** using simple spherical form factor models. However, these attempts failed, as realistic micelle radii did not produce the expected form factor minimum near the (200) reflection. We subsequently fit these scattering data using a core−shell−shell model implemented within the *Irena*[51] software package. In this approach, we modeled the micelles as consisting of a mixed core of H_2SO_4/water surrounded by two concentric shells (Figure S7A). The shells consisted of the protonated tetra(amine) headgroup and associated sulfate counterions (shell 1) and the partially water-solvated hydroxyl groups adjacent to the headgroup (shell 2), which are surrounded by the background "solvent" of hydrophobic tails. Scattering-length densities for the core (SLD_{core}), shell 1 (SLD_{S1}), and shell 2 (SLD_{S2}) were calculated using the electron density contrast calculator in *Irena*. Since the volumetric mass densities of the different regions were unknown, we set physically realistic upper and lower bounds for each quantity as follows. SLD_{core} was modulated between the values for pure H_2SO_4 and pure H_2O, namely, $(9.4-15.9) \times 10^{-10}$ cm^{-2}. SLD_{S1} was calculated to be in the range of $(6.8-10.4) \times 10^{-10}$ cm^{-2} for the $N_2H_2SO_4$ headgroups, assuming a density of 1.0 ± 0.2 g/cm^3. Finally, SLD_{S2} was estimated from the value of 7.67×10^{-10} cm^{-2} for ethanol due to the β-hydroxyl near each amine headgroup, while the hydrophobic tail "solvent" background was treated as having the SLD of *n*-decane (7.14×10^{-10} cm^{-2}). Using these bounded values as fitting parameters, we obtained the optimized SLD values required to obtain a (200) form factor extinction as presented in Figure S7B. The position of the form factor minima for these particles is sensitive to the core and shell radii as well as the scattering-length density of each layer. These fits suggest that the radius of the H_2O-rich core of the FCC micelles is R_{core} = 2.2 Å, with a headgroup shell thickness of R_{S1} = 5.3 Å. This small core radius with respect to the 4.22 nm unit cell parameter concurs with the apparently small size of the reverse micelles in the electron density map (90% isosurface) presented in Figure 4B and is consistent with the very low headgroup hydration measured by composition analysis (vide infra).

In the case of the $\mathbf{1_9}$-**3S** that forms a smaller BCC unit cell, we used the same core−shell−shell form factor model with the same SLD_{core}. Fine-tuning shell 1 and shell 2 SLDs and thicknesses led us to deduce an H_2O-rich micelle core with R_{core} = 2.4 Å (Figure S7C) and a counterion-headgroup shell 1 thickness of R_{S1} = 5.2 Å. The values of SLD_{S1} and SLD_{S2} both had to be increased slightly compared to the previous case in order to render either the (200) or (321) peaks of the BCC scattering pattern extinct in $\mathbf{1_9}$-**3S** and $\mathbf{1_9}$-**1S**, respectively. The internal consistency in the SLD values (within ∼10%) that yield good fits of the FCC and BCC micellar LLC SAXS patterns further supports their validity. Additional evidence for this model is derived from the fact that $\mathbf{1_{10}}$-**1S** prepared in the presence of *n*-dodecane exhibits a swollen FCC unit cell parameter, which drives the appearance of the (200) peak. (See the Experimental Section for sample preparation; SAXS data is given in Figure S8.) In other words, addition of dodecane shifts the position of the (200) peak with respect to the core−shell−shell form factor and leads to its observation by SAXS.

Composition Analyses of Lipidoid LLCs. The above findings provoke the question of how a single, highly hydrophobic molecule with a protonated tetra(amine) headgroup could simultaneously adopt the negative mean curvature required to form a micellar cubic phase and the zero mean curvature required for L_α phase coexistence. To resolve this issue, we sought to determine the extent of amine headgroup protonation in these samples. A combination of gravimetric and elemental analyses was performed on $\mathbf{1_9}$, $\mathbf{1_{10}}$, and $\mathbf{1_{12}}$ LLCs protonated with aqueous HNO_3, H_2SO_4, and H_3PO_4 solutions. (See the Experimental Section for details.)

Detailed composition analyses demonstrate apparent differences in the protonation states of lipidoids $\mathbf{1_n}$ in the presence of different acids (Table 2). $\mathbf{1_{10}}$-**1S** exhibited a molar ratio

https://dx.doi.org/10.1021/acs.langmuir.0c01369
Langmuir 2020, 36, 8240−8252

Table 2. Composition Analyses for Variously Protonated Lipidoid LLCs

sample	morphology[a]	[counterion]/[lipidoid][b]	est. average protonation	mols water/amphiphile[c]
$\mathbf{1_9}$-0.1S	$L_\alpha + I_{II}$	1.8	3.6+	9.5
$\mathbf{1_9}$-1S	I_{II} + dis	2.0	4.0+	6.3
$\mathbf{1_9}$-3N	dis + X	3.3	3.3+	4.2
$\mathbf{1_{10}}$-0.1S	L_α	1.7	3.4+	11
$\mathbf{1_{10}}$-1S	$L_\alpha + I_{II}$	2.0	4.0+	9.3
$\mathbf{1_{10}}$-3N	L_α + X	2.8	2.8+	25
$\mathbf{1_{10}}$-0.5P	L_α + dis	3.0	3.0+	11.6
$\mathbf{1_{12}}$-1S	L_α	2.0	4.0+	13

[a] L_α and I_{II} refer to lamellar and inverse micellar cubic liquid-crystal phases, respectively. "dis" is disordered, and "X" is crystalline. [b] [Counterion]/[$\mathbf{1_n}$] and average protonation state determined by elemental analysis of dried samples. [c] Determined gravimetrically.

[H_2SO_4]:[$\mathbf{1_{10}}$] = 2:1, implying a quadruply protonated TREN headgroup charge balanced by two SO_4^{2-} anions. On the other hand, we deduce that $\mathbf{1_{10}}$-1N exists in a nearly triply protonated state with ∼2.8 NO_3^- anions per lipidoid. In $\mathbf{1_{10}}$-0.5P, elemental analysis indicates the presence of 3 monovalent $H_2PO_4^-$ anions charge-balancing a triply protonated headgroup. This last observation is physically reasonable, considering that 0.5 M H_3PO_4(aq) has pH ∼ 1.26 and the conjugate base would primarily exist in the monovalent $H_2PO_4^-$ form.[73,74] The protonation state of $\mathbf{1_{10}}$ is also acid concentration-dependent: $\mathbf{1_{10}}$-0.1S exhibits 1.7 SO_4^{2-} ions per headgroup, implying that most of TREN headgroups exist in the 3+ state, as compared to $\mathbf{1_{10}}$-1S. Note that the estimated water contents of the pure L_α LLCs ($\mathbf{1_{10}}$-0.5P, $\mathbf{1_{10}}$-0.1S and $\mathbf{1_{12}}$-1S) were greater than that of the pure cubic phase formed by $\mathbf{1_9}$-1S, with intermediate values measured for samples exhibiting L_α/I_{II} phase coexistence ($\mathbf{1_9}$-0.1S and $\mathbf{1_{10}}$-1S).

Overall, these composition analyses reveal strong correlations between the lipidoid protonation state, counterion identity, degree of headgroup hydration, and the resulting supramolecular morphology. Complete protonation is achieved only with H_2SO_4, and only in fully protonated samples were pure I_{II} or L_α/I_{II} LLC phase coexistence observed. The L_α/I_{II} phase coexistence is remarkable, given that the mean interfacial curvatures of these two phases differ dramatically. The flat interfaces of lamellae are best satisfied by cylindrical amphiphile shapes, while the negative curvature of inverse micelles necessitates amphiphile adoption of a truncated conical conformation.[26]

Dichotomous Lipidoid Conformations in LLC Phases. In order to gain deeper insights into the aqueous LLC self-assembly behaviors of protonated lipidoids, we simulated the pure, self-assembled phases of $\mathbf{1_9}$-1S and $\mathbf{1_{12}}$-1S using atomistic molecular dynamics (MD) simulations. (See the Experimental Section for details.) These simulations relied on the experimentally derived unit cell dimensions, headgroup protonation states, and estimated numbers of counterions and water molecules given in Table 2. (See Table S1 for simulation conditions.)

Bias-free MD simulation of $\mathbf{1_9}$-1S using a cubic unit cell with an edge dimension of a = 3.24 nm results in a self-assembled micellar BCC structure (Figure 4C) that resembles the electron density map for this phase (Figure 4A), in which the tetra(amine) headgroups, H_2SO_4, and H_2O are segregated in the micelle cores of the BCC lattice. Bias-free assembly simulations of $\mathbf{1_9}$-1S using the same chemical composition in a smaller unit cell with edge dimension a = 2.31 nm corresponding to an SC structure yielded only a lamellae-like structure. The unstable nature of the SC phase in the simulations concurs with our deduction that the cubic phase is an inverse BCC LLC.

The bias-free self-assembled structure of $\mathbf{1_{12}}$-1S obtained by atomistic MD simulations exhibits the expected alternating L_α layers of hydrophobic lipidoid tails and water with a repeat spacing of d = 2.86 nm (Figure 5A). This spacing agrees well with the experimental d = 2.93 nm. An inspection of van der Waals' representations of individual lipidoids (depicted in red in Figure 5A) in the lamellae demonstrates that they adopt chair-like (chain-extended) conformations in which hydrophobic tails of the same molecule span a single hydrophilic domain to bridge two adjacent hydrophobic bilayers (Figure 5B). This molecular conformation differs significantly from the conventional view of L_α phase self-assembly, wherein the tails of a single amphiphile all reside in the same hydrophobic layer with an average tail orientation coincident with the interface normal. Attempts to bias the MD simulations so that the tails of each protonated $\mathbf{1_{12}}$ lipidoid sit in the same hydrophobic layer, by introducing an attractive interheadgroup interaction, yield equilibrated L_α phases with d = 3.35 nm (Figures 5C and S9; see the Supporting Information for simulation details). This value is more than 0.4 nm (∼13%) larger than the experimental value, suggesting that such conformations are less relevant.

The ability of $\mathbf{1_n}$ lipidoids to adopt the chain-extended conformations depicted in Figure 5A rationalizes the unprecedented coexistence of zero-curvature L_α LLCs with the negative mean curvature inverse micellar FCC phase. If all of the tails are situated on the same side of the headgroup, then the tapered cone conformation drives self-assembly into an inverse micellar structure (Figures 4C and 6). However, the lipidoid can also adopt a chain-extended, chair-like conformation that enables supramolecular packing into a L_α phase. Weiss and co-workers previously implicated related extended-chain conformations of tetra(alkyl)phosphonium salts to explain their ability to robustly form smectic thermotropic liquid crystals.[75,76] Subtle changes to the lipidoid structure and environmental conditions evidently shift the equilibrium between the L_α and I_{II} phases, from which we infer the factors governing their molecular conformations.

Cubic phases are observed only for lipidoids protonated with H_2SO_4(aq), when the fully protonated headgroup (4+) is coordinated with two SO_4^{2-} counterions. On the other hand, protonation with HNO_3(aq) and H_3PO_4(aq) furnishes only L_α phases with triply protonated headgroups. These behaviors may be rationalized in terms of preferred protonated lipidoid conformations that depend on the counterion sizes and stoichiometries, the degrees of counterion-headgroup ion pair dissociation, and counterion electrostatic correlations. In their

https://dx.doi.org/10.1021/acs.langmuir.0c01369
Langmuir 2020, 36, 8240−8252

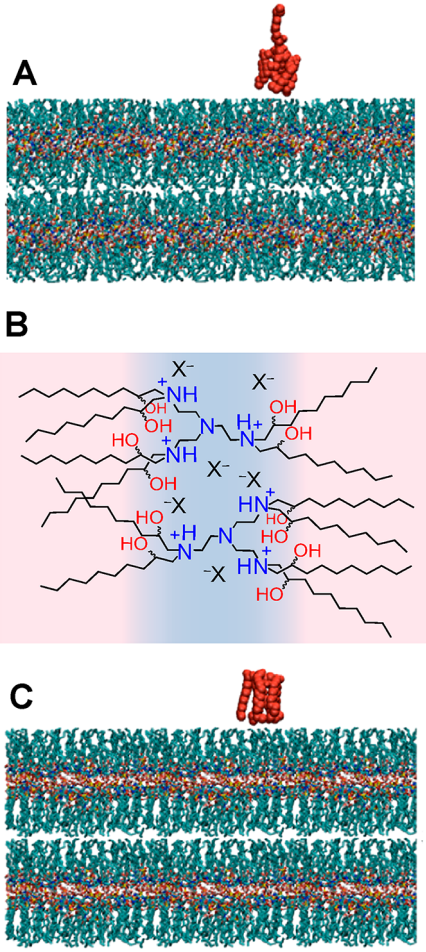

Figure 5. (A) Snapshot of the L_α phase with d = 2.86 nm formed by $\mathbf{1}_{12}$-**1S** in a fully relaxed, bias-free MD simulation with a van der Waals representation of a chain-extended lipidoid conformation (red). (B) Schematic representation of the extended amphiphile conformations within the lamellar phase observed in the bias-free simulation. (C) Snapshot of an L_α phase with d = 3.35 nm formed by $\mathbf{1}_{12}$-**1S** in an MD simulation in which the tail atoms are relaxed but the hydrophilic headgroup interactions have been initially modified with an attractive interaction to bias the tails of each molecule to sit in a single layer, as shown in the van der Waals representation (red).

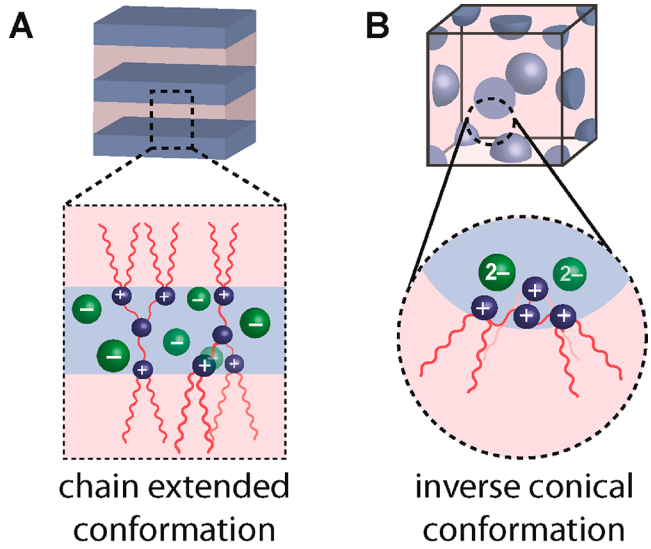

Figure 6. Schematic depiction of protonated lipidoid packings in (A) L_α phases wherein chain-extended conformations are driven by triply protonated headgroups (on average), more dissociated, monovalent counterions, and longer lipidoid alkyl tail lengths and (B) I_{II} LLCs, wherein tetra-protonated ammonium headgroups (on average) with more closely associated divalent counterions enable the formation of an inverse conical conformation in lipidoids with shorter alkyl tail lengths, especially at elevated temperatures and high acid concentrations.

studies of alkyltrimethylammonium surfactants, Liu and Warr demonstrated that multivalent counterions bind more strongly to the hydrophilic/hydrophobic interface due to their greater ability to screen electrostatic repulsions between multiple headgroups.[73,74,77] On this basis, divalent SO_4^{2-} ions are expected to pair more tightly with the tertiary ammonium headgroups as compared to monovalent $H_2PO_4^-$, NO_3^-, and Cl^- ions. In the case of the monovalent ions, the larger number of counterions per protonated lipidoid headgroup exhibit significant packing (steric) and electrostatic interactions. Thus, the lipidoid relieves this combination of packing and electrostatic strain by adopting an extended chain or chair-like conformation to maximize counterion separation around the protonated headgroup (Figure 6A). Thus, monovalent counterions preferentially direct $\mathbf{1}_n$ lipidoids to form L_α phases in which the tails bridge adjacent hydrophobic domains. On the other hand, tighter ion pairing of fewer divalent SO_4^{2-} anions with the protonated lipidoid headgroups more effectively neutralizes their charges with reduced space-filling constraints. Thus, the large hydrophobic volume of the lipidoid tails drives their supramolecular packing into the tighter interfacial curvature aggregates of inverse spherical micelles (Figure 6B).

The lipidoid tail length is another key structural feature that dictates the observed supramolecular morphology: in the homologous series $\mathbf{1}_9$-**1S**, $\mathbf{1}_{10}$-**1S**, and $\mathbf{1}_{12}$-**1S**, a progression from BCC → FCC/L_α coexistence → L_α was observed with increasing tail length when the headgroups were fully protonated (Table 2). These results suggest that longer aliphatic tails (i.e., $n \geq 10$) prefer to adopt the chair-like conformation, which may be rationalized in terms of two different phenomena. Adoption of an inverse cubic micellar structure incurs tail packing frustration[78,79] whereby the tails must stretch to fill space at constant density in a lattice where the micelle interfaces are not equidistant. This tail packing frustration is relieved by adopting a chair-like conformation that drives a lamellar packing, in which variations in lipid tail packing are minimized. Additionally, there is a configurational entropy gain associated with the latter conformation in which the headgroup spans the hydrophilic layer and allows tail anchoring in adjacent hydrophobic domains. Quantitation of the configurational entropy of $\mathbf{1}_{12}$-**1S** in bias-free L_α MD simulations supports this hypothesis (Figure S10). The fully relaxed L_α phase (Figure 5A) exhibits a $-T\Delta S$ term that is 5.6 kJ/mol/tail lower than for the structure in which the tails are forced to sit in a single hydrophobic domain (Figure 5C). Assuming that this entropic contribution to the free energy scales with tail length, short-tail lipidoids likely incur a lower entropy penalty on forming a conical conformation with a fully protonated headgroup, which contributes to their ability to form inverse micellar cubic phases.

A subtle interplay among counterion stoichiometry, hydrated size, and level of dissociation as well as the hydrophobic tail length evidently directs the preferred lipidoid

https://dx.doi.org/10.1021/acs.langmuir.0c01369
Langmuir 2020, 36, 8240−8252

molecular conformations that drive supramolecular self-assembled phase selection. At first glance, the phase behavior appears to contradict conventional wisdom relating amphiphile shape to self-assembly.[26] One might have expected the larger hydrophobic volume occupied by longer aliphatic tails to favor the formation of inverse phases (H_{II} or I_{II}) over L_α. Furthermore, the coexistence of phases with highly negative interfacial curvatures (I_{II}) and zero mean curvature (L_α) is unprecedented on the basis of the expected differences in molecular packing. However, protonated multitail lipidoids exhibit delicate conformational equilibria (Figure 6) that enable rare and unexpected phases to form and to coexist.

■ CONCLUSIONS

We demonstrated that the aqueous lyotropic self-assembly behaviors of a homologous series of six-tail lipidoids ($\mathbf{1}_n$) sensitively depend on the identity of the acid used to protonate their tetra(amine) headgroups. While protonation in HCl(aq), HNO_3(aq), and H_3PO_4(aq) led to crystalline surfactants that in some cases coexist with lyotropic lamellar phases, protonation by H_2SO_4(aq) promoted self-assembly into cubic I_{II} LLCs. Specifically, we unambiguously identified a rare inverse micellar BCC packing ($Im\bar{3}m$ symmetry), in addition to only the second example of an inverse micellar FCC phase ($Fm\bar{3}m$ symmetry). Notably, the FCC phase often coexists with an L_α phase. Microsecond-scale, atomistic MD simulations demonstrate that this unexpected coexistence of phases with dramatically different mean interfacial curvatures is enabled by the ability of these multitail amphiphiles to adopt two distinct conformations. In general, fully protonated tertiary ammonium headgroups closely coordinate two divalent SO_4^{2-} counterions and self-assemble into inverse discontinuous cubic phases in shorter tail lipidoids, while triply protonated headgroups with monovalent counterions and/or longer hydrophobic tails favor L_α phases. LLC materials derived from these bioinspired amphiphiles mimic several features of bacterial lipid A, especially their propensity to self-assemble into lamellar and inverse cubic LLCs in an environment-dependent manner. We anticipate that this fundamental study will lead to future applications of these synthetically accessible lipidoids as bulk, thin film, and particle-based responsive LLCs.

■ ASSOCIATED CONTENT

Supporting Information

The Supporting Information is available free of charge at https://pubs.acs.org/doi/10.1021/acs.langmuir.0c01369.

SAXS and WAXS data for LLCs of $\mathbf{1}_n$**-3C**, $\mathbf{1}_n$**-3N**, $\mathbf{1}_n$**-0.5P**, $\mathbf{1}_n$**-1S**, and $\mathbf{1}_{10}$**-1S** in the presence of dodecane; core−shell−shell form factor fitting details for Le Bail refinements for $\mathbf{1}_9$**-1S** and $\mathbf{1}_{11}$**-3S**; electron density reconstruction method description and input files; and details of molecular dynamics simulations (PDF)

■ AUTHOR INFORMATION

Corresponding Author

Mahesh. K. Mahanthappa − *Department of Chemistry, University of Wisconsin—Madison, Madison, Wisconsin 53706, United States; Department of Chemical Engineering & Materials Science, University of Minnesota, Minneapolis, Minnesota 55455, United States;* orcid.org/0000-0002-9871-804X; Phone: +1 (612) 625−4599; Email: maheshkm@umn.edu

Authors

James Jennings − *Department of Chemistry and Department of Chemical and Biological Engineering, University of Wisconsin—Madison, Madison, Wisconsin 53706, United States;* orcid.org/0000-0003-1213-4607

Matthew C. D. Carter − *Department of Chemistry, University of Wisconsin—Madison, Madison, Wisconsin 53706, United States;* orcid.org/0000-0003-1678-2636

Chang Yun Son − *Department of Chemistry, University of Wisconsin—Madison, Madison, Wisconsin 53706, United States;* orcid.org/0000-0002-0784-6565

Qiang Cui − *Department of Chemistry, University of Wisconsin—Madison, Madison, Wisconsin 53706, United States;* orcid.org/0000-0001-6214-5211

David M. Lynn − *Department of Chemistry and Department of Chemical and Biological Engineering, University of Wisconsin—Madison, Madison, Wisconsin 53706, United States;* orcid.org/0000-0002-3140-8637

Complete contact information is available at: https://pubs.acs.org/10.1021/acs.langmuir.0c01369

Notes

The authors declare no competing financial interest.

■ ACKNOWLEDGMENTS

This work was financially supported by the National Science Foundation Materials Research Science and Engineering Center (MRSEC) at the University of Wisconsin—Madison under DMR-1121288 and CHE-1807330 (M.K.M.) and made use of core user facilities at the University of Wisconsin—Madison partially supported by DMR-1121288, CHE-9974839, and CHE-1048642. Synchrotron SAXS studies were conducted at Sector 12 of the Advanced Photon Source, a U.S. Department of Energy (DOE) Office of Science User Facility operated for the DOE Office of Science by Argonne National Laboratory under contract no. DE-AC02-06CH11357. M.C.D.C acknowledges the Natural Sciences and Engineering Research Council of Canada for a graduate research fellowship.

■ REFERENCES

(1) Senaratne, W.; Andruzzi, L.; Ober, C. K. Self-Assembled Monolayers and Polymer Brushes in Biotechnology: Current Applications and Future Perspectives. *Biomacromolecules* **2005**, *6*, 2427−2448.

(2) van Meer, G.; Voelker, D. R.; Feigenson, G. W. Membrane Lipids: Where They Are and How They Behave. *Nat. Rev. Mol. Cell Biol.* **2008**, *9*, 112−124.

(3) Chu, Z.; Dreiss, C. A.; Feng, Y. Smart Wormlike Micelles. *Chem. Soc. Rev.* **2013**, *42*, 7174−7203.

(4) Ramanathan, M.; Shrestha, L. K.; Mori, T.; Ji, Q.; Hill, J. P.; Ariga, K. Amphiphile Nanoarchitectonics: From Basic Physical Chemistry to Advanced Applications. *Phys. Chem. Chem. Phys.* **2013**, *15*, 10580−10611.

(5) Han, L.; Che, S. Anionic Surfactant Templated Mesoporous Silicas (AMSs). *Chem. Soc. Rev.* **2013**, *42*, 3740−3752.

(6) Faul, C. F. J. Ionic Self-Assembly for Functional Hierarchical Nanostructured Materials. *Acc. Chem. Res.* **2014**, *47*, 3428−3438.

(7) Gu, D.; Schüth, F. Synthesis of Non-Siliceous Mesoporous Oxides. *Chem. Soc. Rev.* **2014**, *43*, 313−344.

(8) Kim, Y.-K.; Noh, J.; Nayani, K.; Abbott, N. L. Soft Matter from Liquid Crystals. *Soft Matter* **2019**, *15*, 6913−6929.

(9) Leal, C.; Bouxsein, N. F.; Ewert, K. K.; Safinya, C. R. Highly Efficient Gene Silencing Activity of siRNA Embedded in a

Nanostructured Gyroid Cubic Lipid Matrix. *J. Am. Chem. Soc.* **2010**, *132*, 16841−16847.
(10) Yoo, J.-W.; Irvine, D. J.; Discher, D. E.; Mitragotri, S. Bio-Inspired, Bioengineered and Biomimetic Drug Delivery Carriers. *Nat. Rev. Drug Discovery* **2011**, *10*, 521−535.
(11) van Rijn, P.; Tutus, M.; Kathrein, C.; Zhu, L.; Wessling, M.; Schwaneberg, U.; Boker, A. Challenges and Advances in the Field of Self-Assembled Membranes. *Chem. Soc. Rev.* **2013**, *42*, 6578−6592.
(12) Martiel, I.; Sagalowicz, L.; Mezzenga, R. Phospholipid-Based Nonlamellar Mesophases for Delivery Systems: Bridging the Gap between Empirical and Rational Design. *Adv. Colloid Interface Sci.* **2014**, *209*, 127−143.
(13) Lagny, T. J.; Bassereau, P. Bioinspired Membrane-Based Systems for a Physical Approach of Cell Organization and Dynamics: Usefulness and Limitations. *Interface Focus* **2015**, *5*, 20150038.
(14) Kim, H.; Leal, C. Cuboplexes: Topologically Active siRNA Delivery. *ACS Nano* **2015**, *9*, 10214−10226.
(15) Palivan, C. G.; Goers, R.; Najer, A.; Zhang, X.; Car, A.; Meier, W. Bioinspired Polymer Vesicles and Membranes for Biological and Medical Applications. *Chem. Soc. Rev.* **2016**, *45*, 377−411.
(16) Mezzenga, R.; Seddon, J. M.; Drummond, C. J.; Boyd, B. J.; Schröder-Turk, G. E.; Sagalowicz, L. Nature-Inspired Design and Application of Lipidic Lyotropic Liquid Crystals. *Adv. Mater.* **2019**, *31*, 1900818.
(17) Seddon, J. M.; Ces, O.; Templer, R. H.; Mannock, D. A.; McElhaney, R. N. Structure and Phase Behaviour of Synthetic Glycolipids. *Mol. Cryst. Liq. Cryst.* **2003**, *402*, 77−84.
(18) Hashim, R.; Sugimura, A.; Minamikawa, H.; Heidelberg, T. Nature-Like Synthetic Alkyl Branched-Chain Glycolipids: A Review on Chemical Structure and Self-Assembly Properties. *Liq. Cryst.* **2012**, *39*, 1−17.
(19) Seddon, J. M. Structure of the Inverted Hexagonal (H_{II}) Phase, and Non-Lamellar Phase Transitions of Lipids. *Biochim. Biophys. Acta, Rev. Biomembr.* **1990**, *1031*, 1−69.
(20) Hyde, S. T., Identification of Lyotropic Liquid Crystalline Mesophases. In *Handbook of Applied Surface and Colloid Chemistry*; Holmberg, K., Ed.; John Wiley & Sons, Inc., New York, 2001; Vol. *1*, pp 299−332.
(21) Love, K. T.; Mahon, K. P.; Levins, C. G.; Whitehead, K. A.; Querbes, W.; Dorkin, J. R.; Qin, J.; Cantley, W.; Qin, L. L.; Racie, T.; Frank-Kamenetsky, M.; Yip, K. N.; Alvarez, R.; Sah, D. W. Y.; de Fougerolles, A.; Fitzgerald, K.; Koteliansky, V.; Akinc, A.; Langer, R.; Anderson, D. G. Lipid-Like Materials for Low-Dose, in Vivo Gene Silencing. *Proc. Natl. Acad. Sci. U. S. A.* **2010**, *107*, 1864−1869.
(22) Sun, S.; Wang, M.; Knupp, S. A.; Soto-Feliciano, Y.; Hu, X.; Kaplan, D. L.; Langer, R.; Anderson, D. G.; Xu, Q. Combinatorial Library of Lipidoids for in Vitro DNA Delivery. *Bioconjugate Chem.* **2012**, *23*, 135−140.
(23) Fairhurst, C. E.; Fuller, S.; Gray, J.; Holmes, M. C.; Tiddy, G. J. T. *Handbook of Liquid Crystals*; Wiley-VCH: Weinheim, 1998.
(24) Burrell, J.; Dymond, M. K.; Gillams, R. J.; Parker, D. J.; Langley, G. J.; Labrador, A.; Nylander, T.; Attard, G. S. Using Curvature Power to Map the Domain of Inverse Micellar Cubic Phases: The Case of Aliphatic Aldehydes in 1,2-Dioleoyl-*sn*-Glycero-3-Phosphoethanolamine. *Langmuir* **2017**, *33*, 12804−12813.
(25) Talaikis, M.; Valldeperas, M.; Matulaitienė, I.; Borzova, J. L.; Barauskas, J.; Niaura, G.; Nylander, T. On the Molecular Interactions in Lipid Bilayer-Water Assemblies of Different Curvatures. *J. Phys. Chem. B* **2019**, *123*, 2662−2672.
(26) Israelachvili, J. N.; Mitchell, D. J.; Ninham, B. W. Theory of Self-Assembly of Hydrocarbon Amphiphiles into Micelles and Bilayers. *J. Chem. Soc., Faraday Trans. 2* **1976**, *72*, 1525−1568.
(27) Mezzenga, R. Physics of Self-Assembly of Lyotropic Liquid Crystals. In *Self-Assembled Supramolecular Architectures*; Garti, N., Somasundaran, P., Mezzenga, R., Eds.; John Wiley & Sons, Inc.: Hoboken, NJ, 2012; pp 1−20.
(28) Gin, D. L.; Bara, J. E.; Noble, R. D.; Elliott, B. J. Polymerized Lyotropic Liquid Crystal Assemblies for Membrane Applications. *Macromol. Rapid Commun.* **2008**, *29*, 367−389.
(29) Sorenson, G. P.; Coppage, K. L.; Mahanthappa, M. K. Unusually Stable Aqueous Lyotropic Gyroid Phases from Gemini Dicarboxylate Surfactants. *J. Am. Chem. Soc.* **2011**, *133*, 14928−14931.
(30) Perroni, D. V.; Baez-Cotto, C. M.; Sorenson, G. P.; Mahanthappa, M. K. Linker Length-Dependent Control of Gemini Surfactant Aqueous Lyotropic Gyroid Phase Stability. *J. Phys. Chem. Lett.* **2015**, *6*, 993−998.
(31) Shearman, G. C.; Tyler, A. I. I.; Brooks, N. J.; Templer, R. H.; Ces, O.; Law, R. V.; Seddon, J. M. Ordered Micellar and Inverse Micellar Lyotropic Phases. *Liq. Cryst.* **2010**, *37*, 679−694.
(32) Lewis, R. N. A. H.; McElhaney, R. N. The Physicochemical Properties of Cardiolipin Bilayers and Cardiolipin-Containing Lipid Membranes. *Biochim. Biophys. Acta, Biomembr.* **2009**, *1788*, 2069−2079.
(33) Som, A.; Yang, L.; Wong, G. C. L.; Tew, G. N. Divalent Metal Ion Triggered Activity of a Synthetic Antimicrobial in Cardiolipin Membranes. *J. Am. Chem. Soc.* **2009**, *131*, 15102−15103.
(34) Unsay, J. D.; Cosentino, K.; Subburaj, Y.; García-Sáez, A. J. Cardiolipin Effects on Membrane Structure and Dynamics. *Langmuir* **2013**, *29*, 15878−15887.
(35) Seydel, U.; Brandenburg, K.; Koch, M. H. J.; Rietschel, E. T. Supramolecular Structure of Lipopolysaccharide and Free Lipid-A under Physiological Conditions as Determined by Synchrotron Small-Angle X-Ray Diffraction. *Eur. J. Biochem.* **1989**, *186*, 325−332.
(36) Brandenburg, K.; Koch, M. H. J.; Seydel, U. Phase-Diagram of Lipid-A from *Salmonella minnesota* and *Escherichia coli* Rough Mutant Lipopolysaccharide. *J. Struct. Biol.* **1990**, *105*, 11−21.
(37) Brandenburg, K.; Seydel, U.; Schromm, A. B.; Loppnow, H.; Koch, M. H. J.; Rietschel, E. T. Conformation of Lipid A, the Endotoxic Center of Bacterial Lipopolysaccharide. *J. Endotoxin Res.* **1996**, *3*, 173−178.
(38) Molinaro, A.; Holst, O.; Di Lorenzo, F.; Callaghan, M.; Nurisso, A.; D'Errico, G.; Zamyatina, A.; Peri, F.; Berisio, R.; Jerala, R.; Jimenez-Barbero, J.; Silipo, A.; Martin-Santamaria, S. Chemistry of Lipid A: At the Heart of Innate Immunity. *Chem. - Eur. J.* **2015**, *21*, 500−519.
(39) Steimle, A.; Autenrieth, I. B.; Frick, J.-S. Structure and Function: Lipid A Modifications in Commensals and Pathogens. *Int. J. Med. Microbiol.* **2016**, *306*, 290−301.
(40) Jacobson, K.; Papahadjopoulos, D. Phase Transitions and Phase Separations in Phospholipid Membranes Induced by Changes in Temperature, pH, and Concentration of Bivalent Cations. *Biochemistry* **1975**, *14*, 152−161.
(41) Brandenburg, K.; Mayer, H.; Koch, M. H. J.; Weckesser, J.; Rietschel, E. T.; Seydel, U. Influence of the Supramolecular Structure of Free Lipid A on Its Biological Activity. *Eur. J. Biochem.* **1993**, *218*, 555−563.
(42) Reichelt, H.; Faunce, C. A.; Paradies, H. H. The Phase Diagram of Charged Colloidal Lipid A-Diphosphate Dispersions. *J. Phys. Chem. B* **2008**, *112*, 3290−3293.
(43) Faunce, C. A.; Paradies, H. H. Two New Colloidal Crystal Phases of Lipid A-Monophosphate: Order-to-Order Transition in Colloidal Crystals. *J. Chem. Phys.* **2009**, *131*, 244708.
(44) Faunce, C. A.; Reichelt, H.; Paradies, H. H. Studies on Structures of Lipid A-Monophosphate Clusters. *J. Chem. Phys.* **2011**, *134*, 104902.
(45) Faunce, C. A.; Paradies, H. H. Phase Transformations in Lipid A-Diphosphate Initiated by Sodium Hydroxide. *J. Phys. Chem. B* **2012**, *116*, 12997−13009.
(46) Faunce, C. A.; Paradies, H. H. Two Dimensional Crystallization of Three Solid Lipid A-Diphosphate Phases. *J. Phys. Chem. B* **2014**, *118*, 800−811.
(47) Brandenburg, K.; Koch, M. H. J.; Seydel, U. Phase-Diagram of Deep Rough Mutant Lipopolysaccharide from *Salmonella minnesota* R595. *J. Struct. Biol.* **1992**, *108*, 93−106.
(48) Lin, I. H.; Miller, D. S.; Bertics, P. J.; Murphy, C. J.; de Pablo, J. J.; Abbott, N. L. Endotoxin-Induced Structural Transformations in Liquid Crystalline Droplets. *Science* **2011**, *332*, 1297−1300.

(49) Carter, M. C. D.; Miller, D. S.; Jennings, J.; Wang, X.; Mahanthappa, M. K.; Abbott, N. L.; Lynn, D. M. Synthetic Mimics of Bacterial Lipid A Trigger Optical Transitions in Liquid Crystal Microdroplets at Ultra Low Picogram-Per-Milliliter Concentrations. *Langmuir* **2015**, *31*, 12850−12855.
(50) Tremblay, A. E.; Whittle, E.; Buist, P. H.; Shanklin, J. Stereochemistry of Δ^4 Dehydrogenation Catalyzed by an Ivy (*Hedera helix*) DΔ^9 Desaturase Homolog. *Org. Biomol. Chem.* **2007**, *5*, 1270−1275.
(51) Ilavsky, J.; Jemian, P. R. *Irena*: Tool Suite for Modeling and Analysis of Small-Angle Scattering. *J. Appl. Crystallogr.* **2009**, *42*, 347−353.
(52) Petříček, V.; Dušek, M.; Palatinus, L. Crystallographic Computing System *JANA2006*: General Features. *Z. Kristallogr. - Cryst. Mater.* **2014**, *229*, 345−352.
(53) Sorenson, G. P.; Schmitt, A. K.; Mahanthappa, M. K. Discovery of a Tetracontinuous, Aqueous Lyotropic Network Phase with Unusual 3D-Hexagonal Symmetry. *Soft Matter* **2014**, *10*, 8229−8235.
(54) Baez-Cotto, C. M.; Mahanthappa, M. K. Micellar Mimicry of Intermetallic C14 and C15 Laves Phases by Aqueous Lyotropic Self-Assembly. *ACS Nano* **2018**, *12*, 3226−3234.
(55) Jayaraman, A.; Mahanthappa, M. K. Counterion-Dependent Access to Low-Symmetry Lyotropic Sphere Packings of Ionic Surfactant Micelles. *Langmuir* **2018**, *34*, 2290−2301.
(56) Palatinus, L.; Chapuis, G. *SUPERFLIP* - a Computer Program for the Solution of Crystal Structures by Charge Flipping in Arbitrary Dimensions. *J. Appl. Crystallogr.* **2007**, *40*, 786−790.
(57) Momma, K.; Izumi, F. *VESTA* 3 for Three-Dimensional Visualization of Crystal, Volumetric and Morphology Data. *J. Appl. Crystallogr.* **2011**, *44*, 1272−1276.
(58) Pronk, S.; Páll, S.; Schulz, R.; Larsson, P.; Bjelkmar, P.; Apostolov, R.; Shirts, M. R.; Smith, J. C.; Kasson, P. M.; van der Spoel, D.; Hess, B.; Lindahl, E. Gromacs 4.5: A High-Throughput and Highly Parallel Open Source Molecular Simulation Toolkit. *Bioinformatics* **2013**, *29*, 845−854.
(59) Schuler, L. D.; Daura, X.; van Gunsteren, W. F. An Improved GROMOS96 Force Field for Aliphatic Hydrocarbons in the Condensed Phase. *J. Comput. Chem.* **2001**, *22*, 1205−1218.
(60) Vanommeslaeghe, K.; Hatcher, E.; Acharya, C.; Kundu, S.; Zhong, S.; Shim, J.; Darian, E.; Guvench, O.; Lopes, P.; Vorobyov, I.; Mackerell, A. D. CHARMM General Force Field: A Force Field for Drug-Like Molecules Compatible with the CHARMM All-Atom Additive Biological Force Fields. *J. Comput. Chem.* **2009**, *31*, 671−690.
(61) Ishiyama, T.; Morita, A. Molecular Dynamics Simulation of Sum Frequency Generation Spectra of Aqueous Sulfuric Acid Solution. *J. Phys. Chem. C* **2011**, *115*, 13704−13716.
(62) Berendsen, H. J. C.; Postma, J. P. M.; van Gunsteren, W. F.; Hermans, J. Interaction Models for Water in Relation to Protein Hydration. In *Intermolecular Forces: Proceedings of the Fourteenth Jerusalem Symposium on Quantum Chemistry and Biochemistry*; Jerusalem, Israel, April 13−16, 1981 Pullman, B., Ed.; Springer Netherlands: Dordrecht, 1981; pp 331−342.
(63) Berendsen, H. J. C.; Postma, J. P. M.; van Gunsteren, W. F.; DiNola, A.; Haak, J. R. Molecular Dynamics with Coupling to an External Bath. *J. Chem. Phys.* **1984**, *81*, 3684−3690.
(64) Kampf, N.; Wu, C.; Wang, Y.; Klein, J. A Trimeric Surfactant: Surface Micelles, Hydration-Lubrication, and Formation of a Stable, Charged Hydrophobic Monolayer. *Langmuir* **2016**, *32*, 11754−11762.
(65) Zhou, C.; Wang, F.; Chen, H.; Li, M.; Qiao, F.; Liu, Z.; Hou, Y.; Wu, C.; Fan, Y.; Liu, L.; Wang, S.; Wang, Y. Selective Antimicrobial Activities and Action Mechanism of Micelles Self-Assembled by Cationic Oligomeric Surfactants. *ACS Appl. Mater. Interfaces* **2016**, *8*, 4242−4249.
(66) Fan, Y.; Wang, Y. Self-Assembly and Functions of Star-Shaped Oligomeric Surfactants. *Langmuir* **2018**, *34*, 11220−11241.
(67) Martiel, I.; Sagalowicz, L.; Mezzenga, R. A Reverse Micellar Mesophase of Face-Centered Cubic $Fm\bar{3}m$ Symmetry in Phosphatidylcholine/Water/Organic Solvent Ternary Systems. *Langmuir* **2013**, *29*, 15805−15812.
(68) Martiel, I.; Handschin, S.; Fong, W.-K.; Sagalowicz, L.; Mezzenga, R. Oil Transfer Converts Phosphatidylcholine Vesicles into Nonlamellar Lyotropic Liquid Crystalline Particles. *Langmuir* **2015**, *31*, 96−104.
(69) Shearman, G. C.; Tyler, A. I. I.; Brooks, N. J.; Templer, R. H.; Ces, O.; Law, R. V.; Seddon, J. M. A 3-D Hexagonal Inverse Micellar Lyotropic Phase. *J. Am. Chem. Soc.* **2009**, *131*, 1678−1679.
(70) Callister, W. D.; Rethwisch, D. G. *Materials Science and Engineering: An Introduction*, 8th ed.; John Wiley & Sons: New York, 2009.
(71) Jayaraman, A.; Zhang, D. Y.; Dewing, B. L.; Mahanthappa, M. K. Path-Dependent Preparation of Complex Micelle Packings of a Hydrated Diblock Oligomer. *ACS Cent. Sci.* **2019**, *5*, 619−628.
(72) Chen, L.; Lee, H. S.; Zhernenkov, M.; Lee, S. Martensitic Transformation of Close-Packed Polytypes of Block Copolymer Micelles. *Macromolecules* **2019**, *52*, 6649−6661.
(73) Liu, C. K.; Warr, G. G. Hexagonal Closest-Packed Spheres Liquid Crystalline Phases Stabilised by Strongly Hydrated Counterions. *Soft Matter* **2014**, *10*, 83−87.
(74) Liu, C. K.; Warr, G. G. Self-Assembly of Didodecyldimethylammonium Surfactants Modulated by Multivalent, Hydrolyzable Counterions. *Langmuir* **2015**, *31*, 2936−2945.
(75) Abdallah, D. J.; Robertson, A.; Hsu, H.-F.; Weiss, R. G. Smectic Liquid-Crystalline Phases of Quaternary Group Va (Especially Phosphonium) Salts with Three Equivalent Long *n*-Alkyl Chains. How Do Layered Assemblies Form in Liquid-Crystalline and Crystalline Phases? *J. Am. Chem. Soc.* **2000**, *122*, 3053−3062.
(76) Abdallah, D. J.; Kwait, D. C.; Bachman, R. E.; Weiss, R. G. Organized Arrangements of "Holes" in Ionic Planes: Crystalline Bis[Tetra-Dodecylammonium] Hexafluorosilicate, a Group 15 Salt with Four Long *n*-Alkyl Chains and a Divalent Anion. *Cryst. Growth Des.* **2001**, *1*, 267−270.
(77) Liu, C. K.; Warr, G. G. Resiliently Spherical Micelles of Alkyltrimethylammonium Surfactants with Multivalent, Hydrolyzable Counterions. *Langmuir* **2012**, *28*, 11007−11016.
(78) Anderson, D. M.; Gruner, S. M.; Leibler, S. Geometrical Aspects of the Frustration in the Cubic Phases of Lyotropic Liquid Crystals. *Proc. Natl. Acad. Sci. U. S. A.* **1988**, *85*, 5364−5368.
(79) Duesing, P. M.; Templer, R. H.; Seddon, J. M. Quantifying Packing Frustration Energy in Inverse Lyotropic Mesophases. *Langmuir* **1997**, *13*, 351−359.

https://dx.doi.org/10.1021/acs.langmuir.0c01369
Langmuir 2020, 36, 8240−8252